

Research Article

Multipoint and Multiobjective Optimization of a Centrifugal Compressor Impeller Based on Genetic Algorithm

Xiaojian Li,¹ Zhengxian Liu,¹ and Yujing Lin²

¹Department of Mechanics, Tianjin University, Tianjin 300072, China

²School of Mechanical and Aerospace Engineering, Kingston University London, London SW15 3DW, UK

Correspondence should be addressed to Zhengxian Liu; zxliu@tju.edu.cn

Received 25 July 2017; Accepted 6 September 2017; Published 15 October 2017

Academic Editor: Filippo Ubertini

Copyright © 2017 Xiaojian Li et al. This is an open access article distributed under the Creative Commons Attribution License, which permits unrestricted use, distribution, and reproduction in any medium, provided the original work is properly cited.

The design of high efficiency, high pressure ratio, and wide flow range centrifugal impellers is a challenging task. The paper describes the application of a multiobjective, multipoint optimization methodology to the redesign of a transonic compressor impeller for this purpose. The aerodynamic optimization method integrates an improved nondominated sorting genetic algorithm II (NSGA-II), blade geometry parameterization based on NURBS, a 3D RANS solver, a self-organization map (SOM) based data mining technique, and a time series based surge detection method. The optimization results indicate a considerable improvement to the total pressure ratio and isentropic efficiency of the compressor over the whole design speed line and by 5.3% and 1.9% at design point, respectively. Meanwhile, surge margin and choke mass flow increase by 6.8% and 1.4%, respectively. The mechanism behind the performance improvement is further extracted by combining the geometry changes with detailed flow analysis.

1. Introduction

The reliance on numerical methods in the aerodynamic design process of turbomachinery components has considerably increased in the last decades. Nowadays, Computational Fluid Dynamics (CFD) codes have matured to a level where they are capable of not only providing a substantial insight into the three-dimensional flow field in turbomachines, but also calculating aerodynamic performances of the machines [1–3]. Meanwhile, higher pressure ratio demand, impeller efficiency, and compressor map width are in severe trade-off relations for transonic impellers [4]. Essentially, the aerodynamic design of transonic impellers is a multiobjective problem. It is a challenging task to design a high pressure ratio centrifugal impeller for high efficiency and wide operating range at the same time [5].

In order to obtain better designs and reduce design cost, automated design optimization of centrifugal impeller has received a widespread attention in recent years. Guo et al. [6] conducted an automated design optimization of a high pressure ratio centrifugal impeller by integrating

an evolution algorithm, 3D blade parameterization method, CFD solver technique, and data mining technique. Verstraete et al. [7] combined a genetic algorithm with an artificial neural network (ANN) to optimize a centrifugal compressor. Hyun-Su et al. [8] carried out the optimal design of impeller for a centrifugal compressor under the influence of flow-induced vibration using fluid-structure interaction and response surface method (RSM). Although much progress has been made in this area, the research on the multiobjective design optimization of a blade is still insufficient especially for very high pressure centrifugal impellers, which has to take into account the trade-off among objective functions. In addition, most published optimization design techniques were performed at one single operating point, usually design point, with the danger of serious deterioration of the performance at off-design conditions such as poorer surge margin and smaller swallowing capacity.

The optimization for the whole speed line is even more challenging, especially near surge condition (certain impellers require good efficiency near the surge and most compressors need good surge margin), as CFD convergence

is often not guaranteed under or near such a condition. Demeulenaere et al. [9] performed a multipoint optimization of a turbocharger compressor wheel. They simulated entire compressor stage including diffuser and housing with significantly increased computational time and effort. Their criterion of surge improvement is higher pressure ratios and the method is open to questions. Pini et al. [10] did a shape optimization of a supersonic turbine cascade at off-design conditions. These two studies propose a pseudoobjective function by summing up all the penalty terms and the original performance objectives with weighting factors, which is not strictly multiobjectives at multipoints. The design variables are so strong and complex to affect the performances that the more variables must be considered in the optimization design. However, there are less analytical expressions available to directly correlate the design variables with the performance at present. Data mining techniques are considered to be able to provide a possible way to extract some useful information from the design space and make the optimization problems in an accessible way. By detecting the features of the data set such as parameter correlations, data mining method can help to gain the mechanism over the performance improvement by optimized designs. Guo et al. [6, 11] applied SOM-based data mining to optimization results of turbomachinery. Jeong et al. [12] conducted a data mining for aerodynamic design space. However, limited research on data mining in turbomachinery design means that the process of data mining and data mining results are still not very clear.

The purpose of this paper is to develop a multipoint and multiobjective design optimization method for high pressure ratio impellers to achieve better aerodynamic performances at both design and off-design conditions and with a wider operating range. The remaining of this paper is organized as follows: first, a time series autoregressive (AR) model is developed to predict surge point from the CFD simulation of a single impeller flow passage and validated by experimental results. A self-organization map (SOM) is then carried out on samples of CFD results to explore the relation between objective functions and design parameters. A total of 27 key design variables selected by the SOM are then employed in the follow-up multiobjective optimization. Finally, the results from the optimization are shown and discussed, and some conclusions and remarks are drawn.

2. Time Series Based Surge Detection

Surge is instability of the centrifugal compressors and is associated with strong unsteadiness of the inlet and outlet pressures and temperatures of the compressor. Therefore, monitoring the time based signal by adopting a Fast Fourier Transform analysis makes it possible to state the instant when the compressor starts to surge and to highlight the typical frequency peak related to surge occurrence [13–15]. However, there is no universal standard for the upper limit of pressure pulsation amplitude in surge detection, making it inconvenient to use. In CFD simulation, though a very accurate CFD model will be the perfect candidate near surge for the rise of numerical instabilities due to the large temporal

and spatial gradients related to the actual flow physics. In real design environment, often only a single impeller flow passage is employed in numerical simulation in order to reduce computational time and effort. As a result, the numerical calculation may become unstable and not convergent before or after real surge because of the simplification made to the real compression system in CFD model. This makes surge detection of a new impeller design or judging the surge margin relative to the baseline impeller difficult.

2.1. Autoregressive Model. Here we propose a new method for surge detection in CFD; it is based on autoregressive (AR) statistical pattern recognition algorithms [16] by monitoring model residual variances. As this paper was first written, we found a similar approach which was employed for early surge warning in axial compressors [17].

The slope of pressure rise is a reliable indicator of compressor stability. If the slope is positive the compressor will be unstable. The maximum or peak compressor pressure ratio thus defines the stability limit. Numerical studies of axial compressors [18, 19] showed that this criterion gives good results in predicting compressor stall. Centrifugal compressors may be able to operate into the left of the peak pressure ratio, but compressors will be in minor surge in this condition [20], and compressor outlet and inlet flow conditions will be pulsating and unsteady. Just like in experimental detection of surge, the unsteadiness of numerical simulation results could be utilized to find the peak compressor pressure ratio and thus help to find stability limit of a compressor.

In the surge detection, one may use the frequencies or amplitude of the unsteady signal. These two parameters are however dimensional so their values depend directly on compressor size and speed, making them unsuitable as universal thresholds in surge detection. By contrast, the time series model methods, such as AR and ARMA, are based on monitoring model residual variances, which is independent of specified compressor impellers and speed.

Autoregression is a data processing technique that is commonly used in constructing a model from time sequence data for extracting underline trends. For a stationary time series x_t ($t = 1, 2, \dots, N$), autoregressive process produces the following results:

$$x_t = \sum_{i=1}^q \phi_i x_{t-i} + a_t \quad a_t \sim \text{NID}(0, \sigma_a^2), \quad (1)$$

where ϕ_i is model coefficients, a_t the random component of the model, and σ_a^2 the variance. If x_t is not zero-mean, then the process can be similarly carried out by introducing a new time series

$$y_t = x_t - \mu_x, \quad (2)$$

where

$$\mu_x = \frac{1}{N} \sum_{i=1}^N x_i \quad (3)$$

is the mean of x_i . The model coefficients, ϕ_i , and the variance, σ_a^2 , can be calculated by the following method:

Autocovariance R_k function,

$$R_k = \frac{1}{N-k} \sum_{t=k+1}^N y_t y_{t-k} \quad (k = 0, 1, 2, \dots, N-1). \quad (4)$$

Coefficients $\mathbf{f} = [\phi_1 \ \phi_2 \ \dots \ \phi_q]^T$ are calculated by

$$\mathbf{f} = (\mathbf{y}^T \mathbf{y})^{-1} \mathbf{y}^T \mathbf{z}, \quad (5)$$

where

$$\mathbf{z} = [y_{q+1} \ y_{q+2} \ \dots \ y_N]^T, \quad (6)$$

$$\mathbf{y} = \begin{bmatrix} y_q & y_{q-1} & \dots & y_1 \\ y_{q+1} & y_q & \dots & y_2 \\ \vdots & \vdots & & \vdots \\ y_{N-1} & y_{N-2} & \dots & y_{N-q} \end{bmatrix}.$$

The variance is given by

$$\sigma_a^2 = \frac{1}{N-q} \sum_{t=q+1}^N \left(y_t - \sum_{i=1}^q \phi_i y_{t-i} \right)^2. \quad (7)$$

By monitoring the variance of compressor unsteady signal, one may judge whether the compressor surges or becomes unstable.

2.2. Surge Detection Method. For the outlet boundary condition, mass flow rate condition is not appropriate as the convergence of CFD cannot be guaranteed near surge condition, resulting in premature sinusoidal waves of flow parameters. Thus, a static pressure condition is adopted and the signal of mass flow rate at LE is monitored. It tends to be a periodic wave but not sinusoidal.

The rise of static pressure at outlet boundary is flattened out near surge condition; a dichotomy or sectional method is applied to the determination of the maximum outlet static pressure near surge condition. This method will be demonstrated in the next section with an example. The flow chart of surge detection is presented in Figure 1. An initial static pressure is specified at impeller outlet before a steady calculation. If this calculation is not convergent, the CFD simulation is switched to unsteady calculation, and the temporal mass flow rate signal at LE is monitored. The AR model is then applied to this time series signal to determine whether the compressor surges at the set pressure level and this is followed by a dichotomy method to find a new static pressure between previous converged steady and present unsteady pressures at the outlet. The detection process continues until a preset minimum pressure rise is reached, and the last steady point is regarded as the last stable point before surge.

TABLE 1: SRV2AB rotor design parameters.

Shaft speed	50000 rpm
Design mass flow rate	2.55 kg/s
Impeller tip radius	112 mm
Diffuser outlet radius	212.8 mm
Rotor tip speed	586 m/s
Rotor pressure ratio	6.2 : 1
Blade number full/splitter	13/13
LE hub radius	30 mm
LE tip radius	78 mm
Blade angle LE tip	26.5 deg (from tangential)
Blade angle TE	52 deg (from tangential)
Exit blade height	8.7 mm
Diffuser inclination against radial	13 deg
Tip clearance	0.5 mm at inlet to 0.3 mm at exit

2.3. Surge Detection of SRV2AB Impeller. This surge detection approach is applied to a higher pressure centrifugal impeller, SRV2AB impeller [21, 22].

The surge detection validation is carried out by the comparison of surge line between CFD prediction and experimental results of the SRV2AB impeller with vaneless diffuser, which serves as the baseline for the subsequent optimization. The basic design parameters of this compressor are given in Table 1.

A mesh independence investigation was firstly conducted by coarse, medium and fine meshes with total mesh number of 0.3, 0.9, and 1.7 million, respectively (for one blade channel). The mesh has a structured H-O topology and the minimum value of y^+ is less than 10. The size of the first cell to wall is 5×10^{-6} m. As shown in Figure 2, the medium mesh seems to provide a good compromise between accuracy and computational efficiency and hence this mesh is used for the rest of the study (see Figure 3), wherein the grid numbers in I, J, K direction is 73, 53, and 201, respectively. The grid number in impeller clearance is 13. The 3D Reynolds-averaged Navier–Stokes (RANS) equations are applied using the commercial software of NUMECA Fine. The Spalart-Allmaras turbulence model, which is highly efficient and suitable for the 3D flow with strong pressure gradient, moderate curvature, and separating flows such as transonic compressor internal flow [11, 23], is adopted to take the turbulence effects into account. The spatial discretization used for the computation is central scheme and the time integration scheme is an explicit four-step Runge-Kutta algorithm.

The sketch of dichotomy to reach the highest outlet static pressure at surge point is shown in Figure 4. For the impellers generated in the optimization process, the outlet static pressure near surge were first set to be 511,300 pa, 521,300 pa, 531,300 pa, and 541,300 pa according to Figure 1. A new value of static pressure was then obtained by dichotomy in between 531,300 pa and 541,300 pa and so on. The smallest step of pressure rise Δp was set to be 200 pa. This value

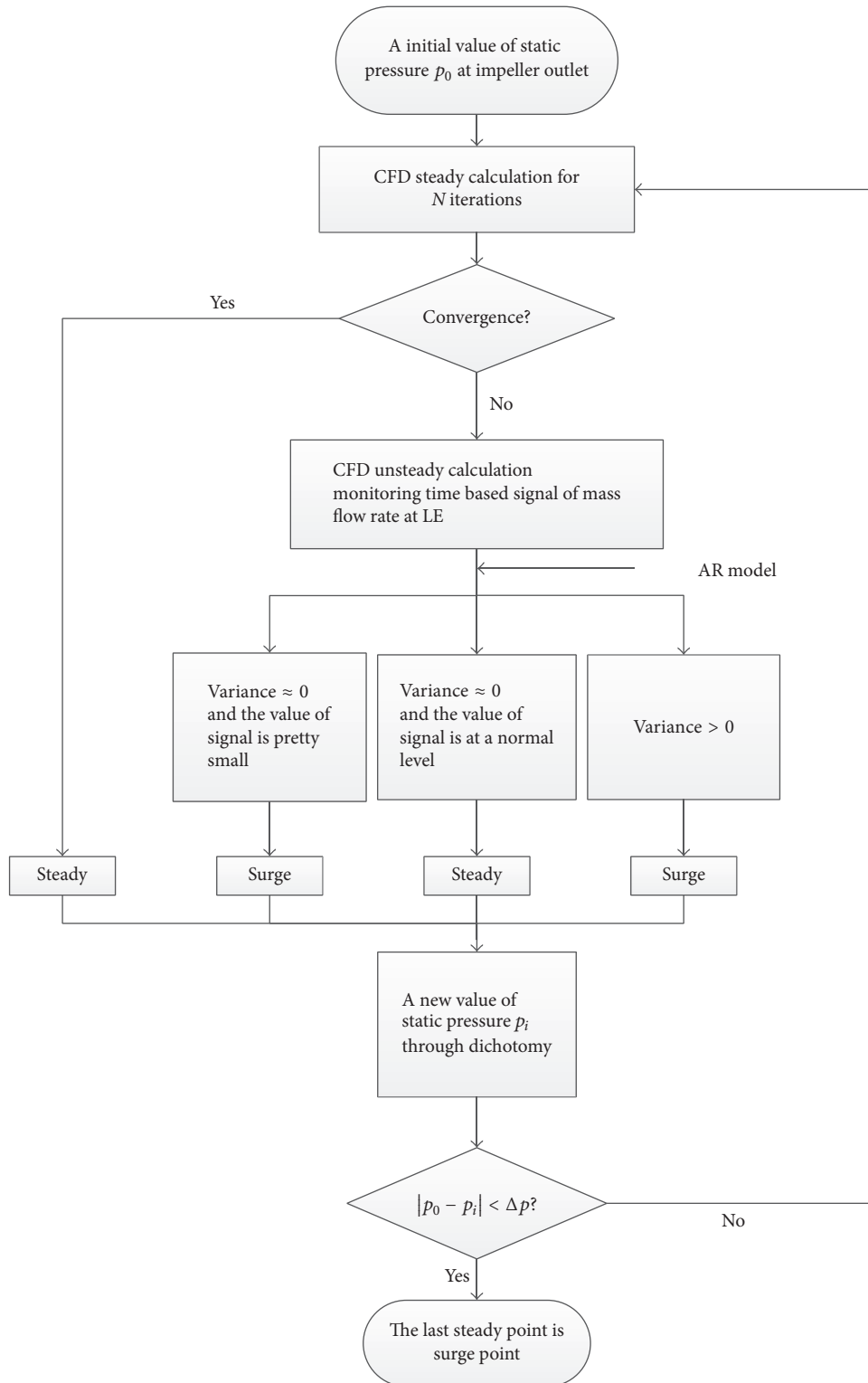


FIGURE 1: The flow chart of surge detection method.

is large but was used to speed up the detection. In order to compensate the effect of a relatively large value of the minimum pressure increment, the surge point was actually located by decreasing the last detected stable mass flow

rate value by 2.5% of the difference between the last two mass flow rates. The corresponding pressure ratio is then evaluated through a third-order polynomial interpolation. In the detection, CFD steady iteration was 2000, the upper

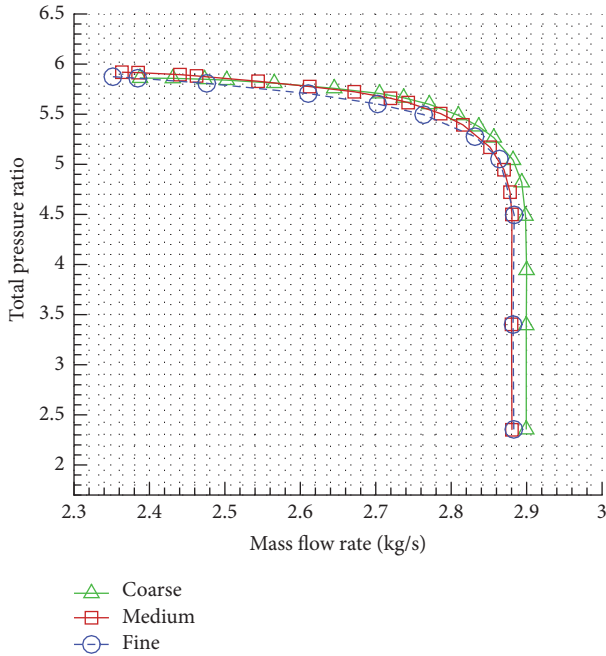


FIGURE 2: Mesh independence investigation.

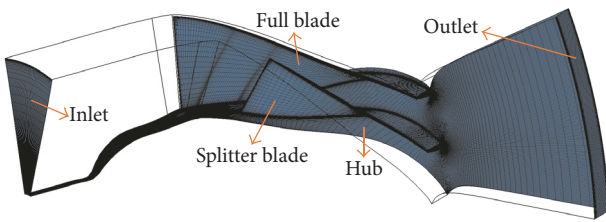


FIGURE 3: Aerodynamic computational domain and grid of SRV2AB (single passage).

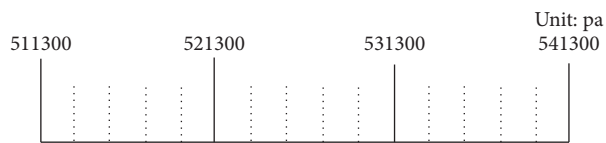


FIGURE 4: The sketch of dichotomy to reach the highest static pressure at surge point.

border of variance was set to be $\delta = 5\%a$. The spatial discretization and time integration schemes applied to the unsteady computation are the same as above in this section. Courant-Friedrich-Levy (CFL) number globally scales the time-step sizes used for the time-marching scheme of the flow solver. A higher value of the CFL number results in a faster convergence but will lead to divergence if the stability limit is exceeded [24]. Typical values of CFL are 1~10 and the maximum CFL number reached in unsteady calculations is set to be 3. The physical time-step size is recommended to be $\Delta t \leq 1/10 \cdot Nb/(n/60)$ for turbomachinery, where n denotes shaft speed (rpm), Nb is blade number [25], and here it is $50/n$ s (equals 0.001 second). The CFL and physical time

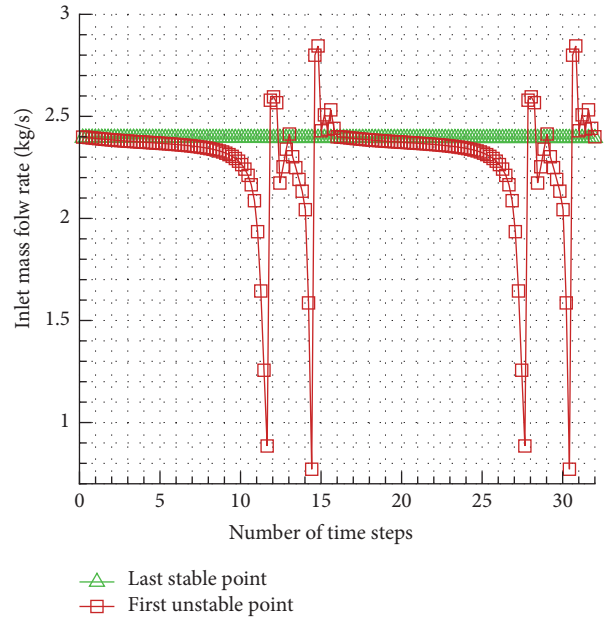


FIGURE 5: Time based mass flow rate signal at LE.

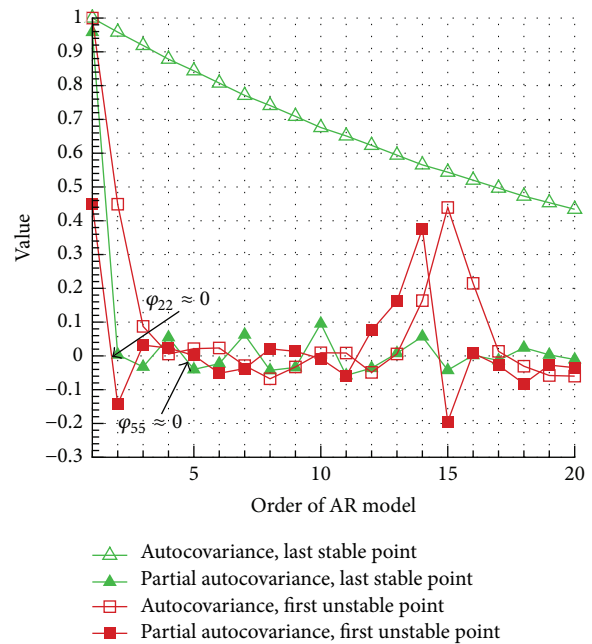


FIGURE 6: Autocovariance and partial autocovariance versus order of AR model.

step seem to provide a good trade-off between computational stability and efficiency after trial.

The time based mass flow rate signals at LE, monitored at the last stable point and the first unstable point for design speed (50000 rpm), are presented in Figure 5. It shows a periodic but not sinusoidal wave for the first unstable point. The autocovariance and partial autocovariance versus order of AR model based on the time signal is given in Figure 6,

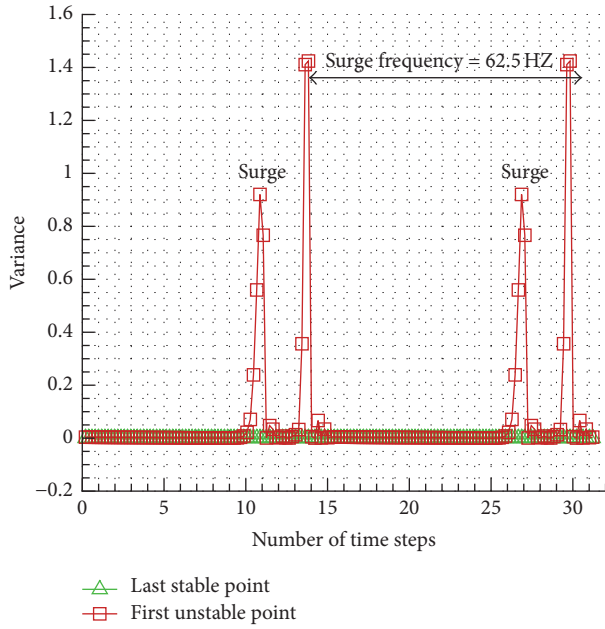


FIGURE 7: Variance versus number of time steps.

where $\varphi_{22} \approx 0$ for the last stable point and $\varphi_{55} \approx 0$ for the first unstable point, which indicates that the AR model is suitable for the time based signals and their order, are $q = 1$ and $q = 4$, respectively. As shown in Figure 7, variance of the time based signal fluctuates periodically for the first unstable point. The distance between two adjacent main peaks shows the surge period (frequency), which is corresponding to the main frequency (largest pulsation amplitude) in the Fast Fourier Transform analysis. The variance of a stable point is about zero, while that for an unstable point fluctuates with large pulsation amplitude, providing a convenient approach to detect instability.

Figure 8 compares predicted and measured surge lines of the SRV2AB impeller with vaneless diffuser at 50,000, 40,000, and 30,000 rpm, corresponding to 100%, 80%, and 60% of design speed. Generally, the prediction matches the experimental results quite well at all operating speeds. This gives confidence in the surge detection method.

3. Data Mining Based on Self-Organizing Map for Optimization of Design Space of SRV2AB

In the turbomachinery design using CFD-based optimization, it is important to determine a small number of key design variables from design space to simplify design problem. The information about the design space, such as trade-off between objective functions, the relations between design variables and objective functions, and why performance of the optimized designs has been improved will be useful for this purpose by eliminating the design variables which do not have a large influence on the objective functions, thereby the efficiency as well as the reliability of optimization process

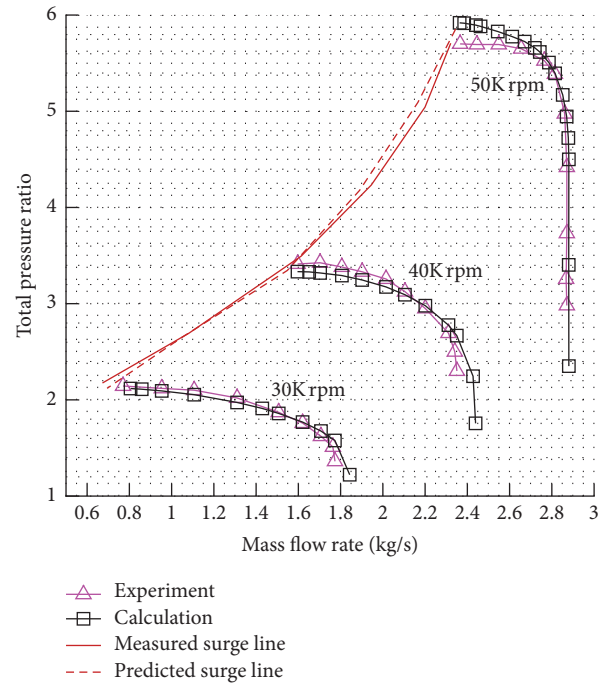


FIGURE 8: Comparison of predicted and measured total pressure ratio of SRV2AB impeller with vaneless diffuser.

may be greatly improved. Furthermore, it is preferable for a designer to provide some alternative or suboptimum solutions for the decision making of the final design. The process to extract information from the design space by detecting the features of the optimization results is called “data mining.” This paper deals with the data mining technique based on SOM.

3.1. Initial Design Variables and Objective Functions. In terms of 3D parameterization of impeller geometry, refer to authors’ previous work [26]. Figure 9 shows the control points of endwalls ((Z, R), two variables for one control point) and blade camber curves (θ , one variable for one control point). For the endwalls, 13 control points are applied to the hub and 8 for the shroud. The blade profile is parameterized by the root and the tip sections of both full and splitter blades (4 sections in total), and other camber sections are determined by linear interpolation from root and tip sections. 8 control points are selected for each full blade section while 5 for each splitter blade section.

Table 2 shows variable names and corresponding numbers of control points. Not all the variables of control points are active in the optimization. Table 3 shows active variable numbers, range of variations, and constraints. In total, 45 design variables are selected for the initial design space according to the constraints of mechanical design of SRV2AB.

The impeller will be optimized at 50000 rpm for maximizing isentropic efficiency and total pressure ratio at design operating condition (2.55 kg/s), while striving for smaller

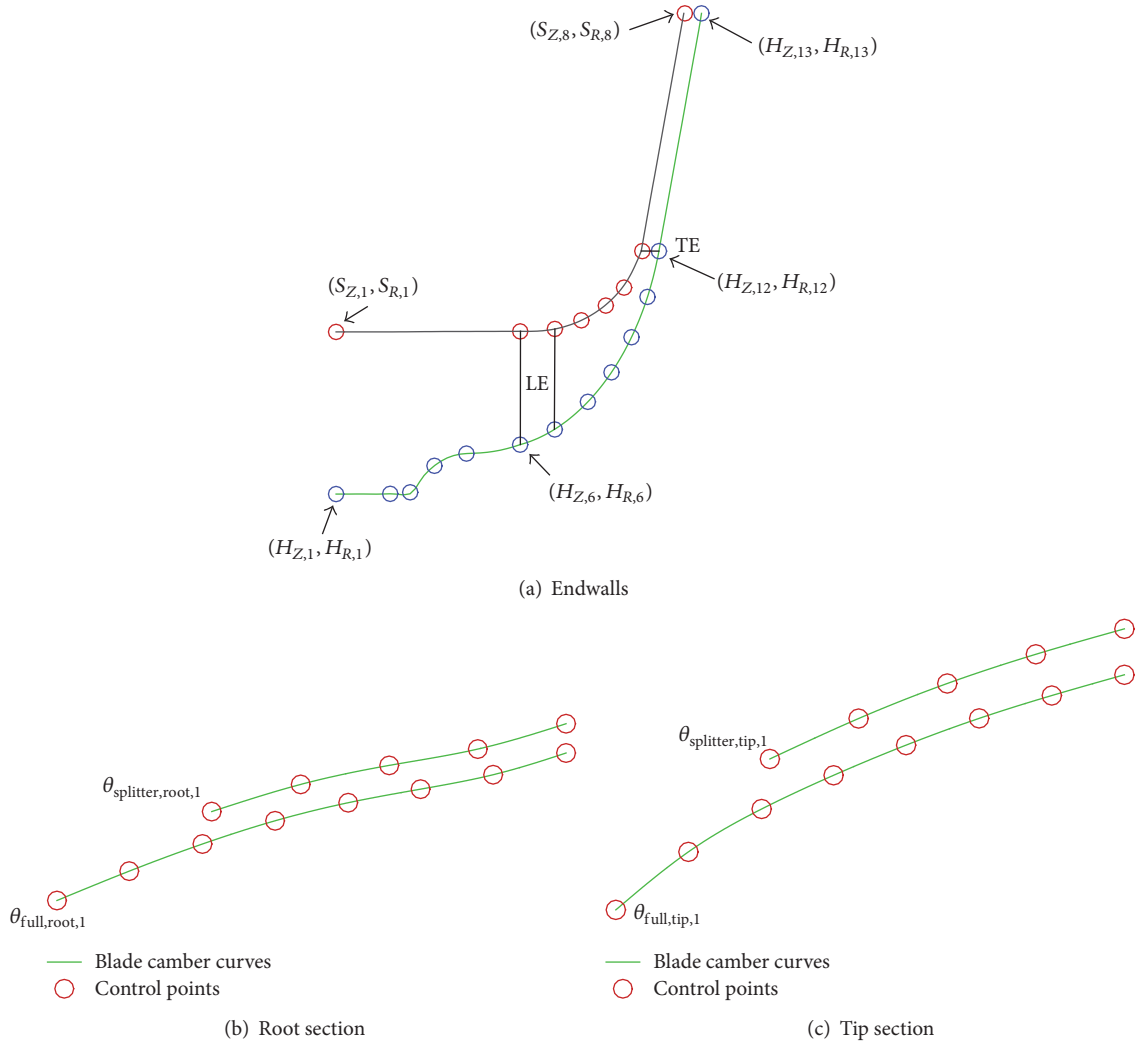


FIGURE 9: Control points of endwalls and blade camber curves.

surge and larger choke mass flows. The corresponding mathematical expression of aerodynamic optimization of SRV2AB is as follows:

$$\begin{aligned}
 \max: & \quad \eta_{is,design}, \varepsilon_{tot,design}, \dot{m}_{choke} \\
 \min: & \quad \dot{m}_{surge} \\
 \text{s.t.}: & \quad n = 50000 \text{ rpm.}
 \end{aligned} \tag{8}$$

3.2. Self-Organization Map. SOM expresses the information in a qualitative way and visualizes not only the relation between design variables and objective functions but also the trade-off between the objective functions. It employs a nonlinear projection algorithm from high to low-dimensions and a clustering technique. This projection is based on self-organization of a low-dimensional array of neurons. In the projection algorithm, the weights between the input vector and the array of neurons are adjusted to represent features of the high-dimensional data on the low-dimensional map. Figure 10 shows the schematic map of SOM, where M is the

TABLE 2: Variable names and corresponding numbers of control points.

Variable name	Variable number
$H_{Z,i}$ ($i = 1, 2, \dots, 13$)	1–13
$H_{R,i}$ ($i = 1, 2, \dots, 13$)	14–26
$S_{Z,i}$ ($i = 1, 2, \dots, 8$)	27–34
$S_{R,i}$ ($i = 1, 2, \dots, 8$)	35–42
$\theta_{full,root,i}$ ($i = 1, 2, \dots, 8$)	43–50
$\theta_{full,tip,i}$ ($i = 1, 2, \dots, 8$)	51–58
$\theta_{splitter,root,i}$ ($i = 1, 2, \dots, 5$)	59–63
$\theta_{splitter,tip,i}$ ($i = 1, 2, \dots, 5$)	64–68

number of neurons and n is equal to the dimension of input vector. Each neuron is connected to adjacent neurons by a neighborhood relation and usually forms two-dimensional hexagonal (see Figure 10(b)) topology.

The learning algorithm of SOM starts with finding the best-matching unit (winning neuron) which is closest to the

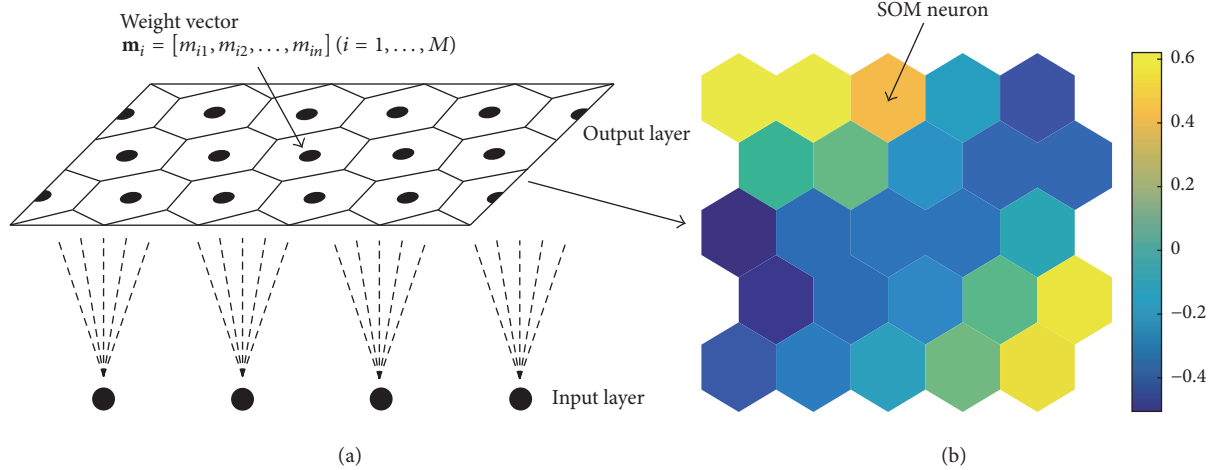


FIGURE 10: Schematic map of SOM.

TABLE 3: Active variable numbers, range of variations, and constraints in initial design space.

	Active variable number	Range of variation
	7, 8, 9, 10, 11	$(-1\% \sim 1\%) (H_{Z,13} - H_{Z,1})$
Hub	20, 21, 22, 23, 24	$(-1\% \sim 1\%) (H_{R,13} - H_{R,1})$
	29, 30, 31, 32, 33, 34	$(-1\% \sim 1\%) (S_{Z,13} - S_{Z,1})$
Shroud	37, 38, 39, 40	$(-1\% \sim 1\%) (S_{R,13} - S_{R,1})$
	44, 45, 46, 47, 48, 49, 50	$(-3\% \sim 3\%) \cdot (\theta_{full,root,8} - \theta_{full,root,1})$
Full root	51, 52, 53, 54, 55, 56, 57, 58	$(-3\% \sim 3\%) \cdot (\theta_{full,tip,8} - \theta_{full,tip,1})$
Full tip	59, 60, 61, 62, 63	$(-3\% \sim 3\%) \cdot (\theta_{splitter,root,5} - \theta_{splitter,root,1})$
Splitter root	64, 65, 66, 67, 68	$(-3\% \sim 3\%) \cdot (\theta_{splitter,tip,5} - \theta_{splitter,tip,1})$
Splitter tip		

Constraints. (1) Inactive variables are unchanged in the optimization. (2) Diffuser inclination against radial equals 13 deg. (3) Shaft speed is 50000 rpm.

input vector \mathbf{x} , and the j th winning neuron is selected as the one having minimal distance value:

$$\|\mathbf{x} - \mathbf{m}_j\| = \min \|\mathbf{x} - \mathbf{m}_k\| \quad (k = 1, \dots, M). \quad (9)$$

Once the best-matching unit is determined, the weight vectors are adjusted not only for the best-matching unit but also for its neighbors. As shown in Figure 11, based on the distance, the best-matching unit and its neighboring neurons (situated on the cross of the solid lines, the weight vectors of neurons represent their locations) become closer to the input vector \mathbf{x} . The adjusted topology is represented with dashed

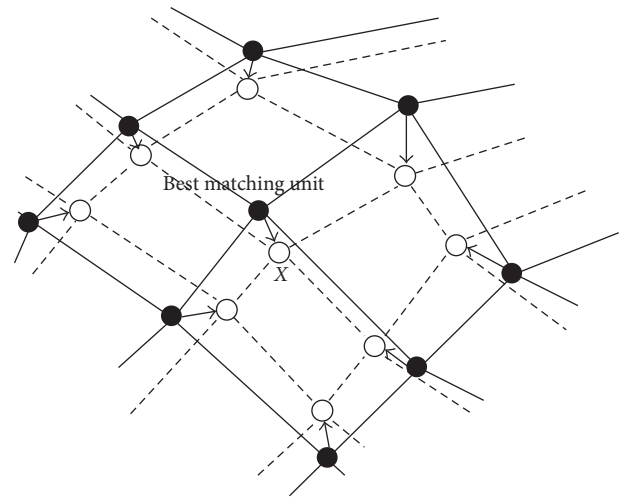


FIGURE 11: Adjustment of the best-matching unit and its neighbors.

lines. The adjustment of weight vector near the best-matching unit can be formulated as follows:

$$\mathbf{m}_k(t+1) = \mathbf{m}_k(t) + h_j(N_j(t), t) (\mathbf{x} - \mathbf{m}_k) \quad (10)$$

$$k = 1, 2, \dots, M,$$

where $\mathbf{m}_k(t)$ is the weight vector of the k th neuron at t iteration. The amount of adjustment depends on the degree of similarity between a neuron and the input, represented by $(\mathbf{x} - \mathbf{m}_k)$, and is scaled by the function $h_j(N_j(t), t)$ that plays the role of a "learning rate." This "learning rate" is called the neighborhood kernel [27]. It is a function of both time (iteration step) and the winning neuron spatial neighborhood $N_j(t)$. This spatial neighborhood is a time-dependent function that defines the set of neurons that are topographically close to the winning neuron. The neurons in the spatial neighborhood adjust their weights according to the same learning rule but with amounts depending on their position with respect to the winner.

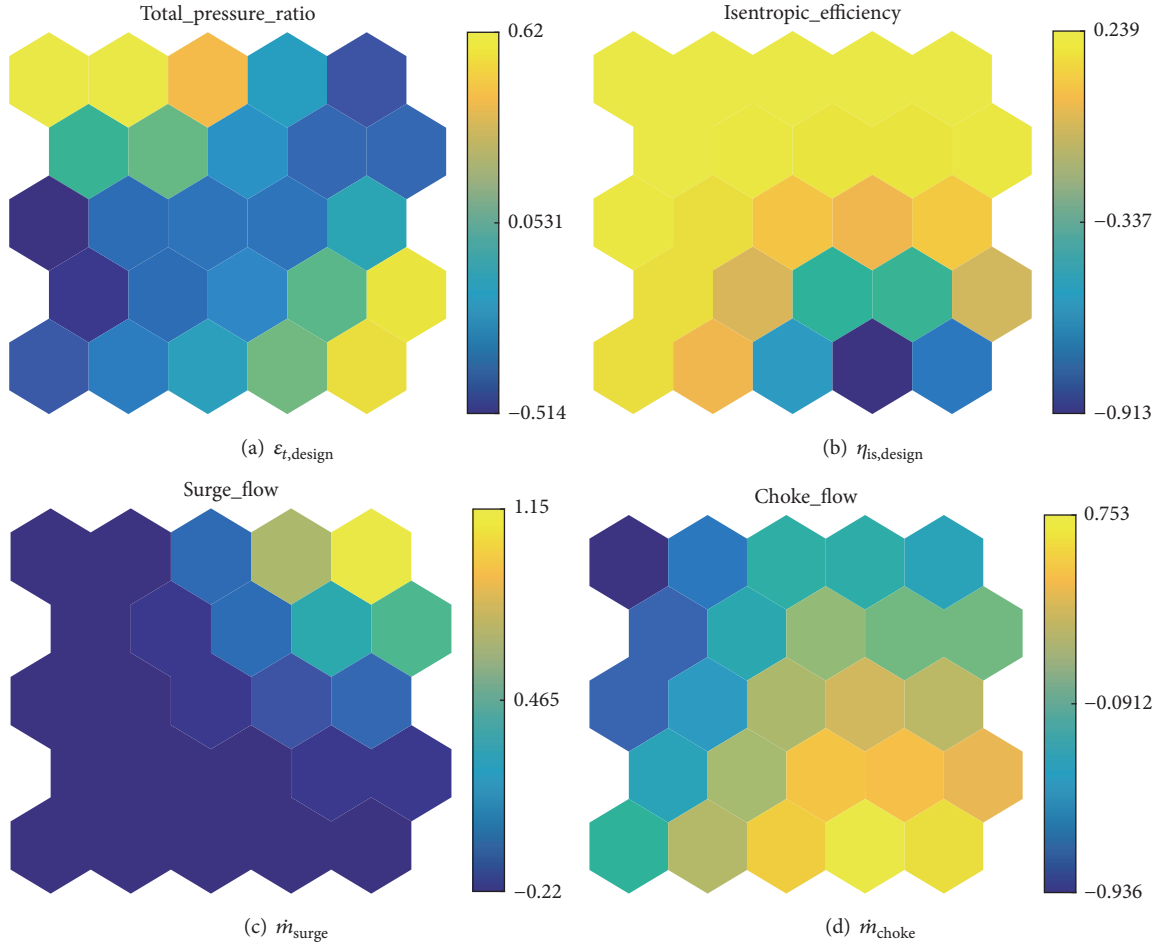


FIGURE 12: SOMs colored by objective functions of initial design space.

Repeating this learning algorithm, the weight vectors become smooth not only locally but also globally. Thus, the sequence of the vectors in the original space results in a sequence of the corresponding neighboring neurons in the two-dimensional map.

Once the high-dimensional data projected on the two-dimensional regular grid, the map can be used for visualization and data mining. The same location on each component map corresponds to the same SOM neuron, which is colored according to its related neuron component values. By comparing the behavior of the color pattern in the same region, one can analyze the correlations among parameters. Parameters are correlated if there exist similar color patterns in the same region of the corresponding component maps.

3.3. SOM-Based Data Mining for Choosing Design Space. The SOM was carried out by an in-house code on initial design space to select key design parameters in the design space for further optimization. 100 impellers generated in random were simulated, in which 49 parameters (4 objectives and 45 active design variables) were analyzed. All the employed parameters are normalized (variance is normalized to one). 25 SOM neurons were used in component map. Figure 12

presents SOMs colored by 4 objective functions, showing a nonlinear relation; no region exists with good performance for all the objectives. This means that it is difficult to improve all the objectives without any compromise. A trade-off needs to make among the 4 objectives. For example, the clusters in bottom right-hand corner are a better choice for total pressure ratio $\epsilon_{\text{tot,design}}$, surge mass flow \dot{m}_{surge} , and choke mass flow \dot{m}_{choke} , but bad in isentropic efficiency $\eta_{\text{is,design}}$. SOMs colored by $\eta_{\text{is,design}}$ and \dot{m}_{choke} show an inverse distribution of colors, so they are in a severe trade-off relation. One physical example is a high trim impeller which has a large choke flow but tends to have low peak efficiency. Another potential conflict of objectives involves \dot{m}_{surge} and $\eta_{\text{is,design}}$. SOM colored by $\epsilon_{\text{tot,design}}$ on the other hand shows diagonal behavior.

Figure 13 shows SOMs for some active design variables in the initial design space. Variable 33 (Figure 13(c)) represents $S_{Z,7}$ and controls the exit blade height of impeller. Larger value of variable 33 means smaller blade tip width and vice versa (refer to Figure 9). The cluster with small values of variable 33 is located in the bottom right-hand corner and brings good performance of $\epsilon_{\text{tot,design}}$, \dot{m}_{surge} , and \dot{m}_{choke} but deteriorates $\eta_{\text{is,design}}$. The largest value of variable 33

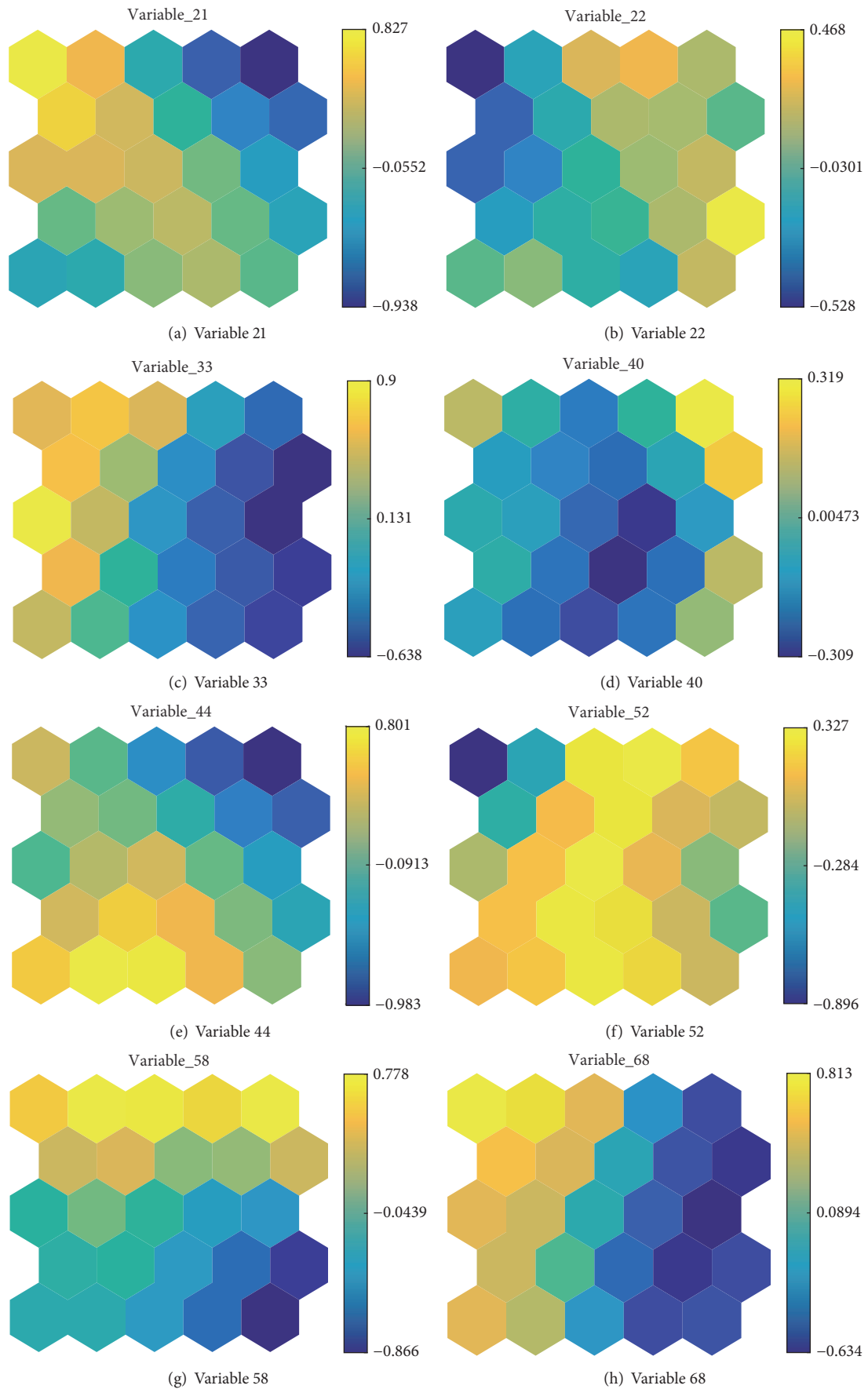


FIGURE 13: SOMs colored by active design variables of initial design space.

situates on middle left and benefits $\eta_{is,design}$ and \dot{m}_{surge} , while penalizing $\epsilon_{tot,design}$ and \dot{m}_{choke} . Figure 13(f), combined with Figure 12, shows the influence of variable 52 or $\theta_{full,tip,2}$ which is the wrap angle of full blade at tip section. Figure 13(e) (variable 44, $\theta_{full,root,2}$) indicates the influence of the wrap angle of full blade at root section. It shows an approximate inverse distribution of color pattern with \dot{m}_{surge} , indicating a positive correlation between increasing value of variable 44 and decreasing \dot{m}_{surge} . Variable 58 (Figure 13(g)) represents $\theta_{full,tip,8}$ which governs the back sweep of full blade at tip section (large value of variable 58 represents large sweepback). SOMs colored by variable 58 and $\eta_{is,design}$ show similar color patterns, implying an approximate linear relation between the two. Both smaller and larger values of variable 58 (located in bottom right-hand and upper left-hand corner, resp.) bring good performance of $\epsilon_{tot,design}$; this is due to smaller sweepback tending to increase the tangential component of absolute velocity to raise total pressure while larger sweepback tries to achieve the same by improving efficiency. Figure 13(h) (variable 68, $\theta_{splitter,tip,5}$) shows the similar effects. Variable 21 (Figure 13(a)), variable 22 (Figure 13(b)), and variable 40 (Figure 13(d)) show severe nonlinear relations with the four objective functions, while variable 22 and variable 40 are more sensitive as the ranges of legends in Figures 13(b) and 13(d) are small. Thus, variable 22 and variable 40 are kept while variable 21 is ignored in the final design space.

Based on data mining results, one may derive the following conclusions. (1) Total pressure ratio, isentropic efficiency, surge mass flow, and choke mass flow are in severe trade-off relations and compromises are needed in optimization. (2) The performance of high pressure ratio impellers is sensitive to the tip and root sections parameters located near the leading edge of full blade, especially for surge margin. The parameters located near the trailing edge of full and splitter blades also have large effects on the performance. The ranges of the control points of these parameters in optimization need careful planning. (3) Some insensitive variables may be ignored in the design space to simplify the optimization and to improve the efficiency as well as the robustness of optimization.

Table 4 shows the active variables and their ranges in the final design space that were used in the optimization. The number of active variables reduces from 45 to 27. Figure 14 presents active variables of endwalls and blade camber curves in final design space, in which the arrows indicate the moving directions of the active variable in the optimization.

4. Aerodynamic Optimization of SRV2AB

4.1. Optimization Method. A multipoint and multiobjective design optimization method based on an improved NSGA-II genetic algorithm [26], the time series surge detection, and data mining technique discussed earlier is applied to the optimization of SRV2AB impeller at design shaft speed (50000 rpm). The four objectives are higher efficiency, pressure ratio, larger choke flow, and smaller surge flow. A Pareto-based ranking was adopted for the 4 objectives.

The flow chart of this multipoint and multiobjective design optimization method is shown in Figure 15. The

TABLE 4: Active variable numbers and range of variations in final design space.

	Active variable number	Range of variation
Hub	9, 10	(-1%~1%) ($H_{Z,13} - H_{Z,1}$)
	20, 22, 23	(-1%~1%) ($H_{R,13} - H_{R,1}$)
Shroud	31, 32, 33	(-1%~1%) ($S_{Z,13} - S_{Z,1}$)
	39, 40	(-1%~1%) ($S_{R,13} - S_{R,1}$)
Full root	44, 45, 46, 48, 50	(-3%~3%) · ($\theta_{full,root,8} - \theta_{full,root,1}$)
Full tip	52, 53, 54, 55, 58	(-3%~3%) · ($\theta_{full,tip,8} - \theta_{full,tip,1}$)
Splitter root	59, 61, 63	(-3%~3%) · ($\theta_{splitter,root,5} - \theta_{splitter,root,1}$)
Splitter tip	64, 65, 67, 68	(-3%~3%) · ($\theta_{splitter,tip,5} - \theta_{splitter,tip,1}$)

Constraints. (1) Same as in Table 3.

TABLE 5: Settings of the genetic algorithm & CFD.

Population size	30
Maximum iteration number	20
Crossover probability P_{c1}	0.9
Crossover probability P_{c2}	0.3
Mutation probability P_{m1}	0.2
Mutation probability P_{m2}	0.05
Convergence criterion of CFD	10^{-5}

right-hand part of the chart presents the core optimization algorithm based on the genetic algorithm. The grid generation and CFD solution were automatically carried out using Autogrid and FineTurbo from NUMECA by templates, respectively. The prediction of total pressure ratio and isentropic efficiency at design operating condition was conducted by imposing design mass flow (2.55 kg/s) boundary condition at vaneless diffuser outlet. Choke mass flow rate was obtained by specifying a low outlet static pressure of 151,300 pa. The determination of surge mass flow is carried out by the surge detection method introduced earlier. The initial design space is presented in Table 3, and the final design space in Table 4. Table 5 shows some essential parameters in the genetic algorithm. Parallel computing technique was applied to the optimization process. It included parallel CFD tool and the multithreaded genetic algorithm in which the parallel CFD code runs. The optimization was carried out on a workstation with 48-core Xeon(R) E5-2670 processor, and the CPU utilization was about 86 percent. The total computational time required to run the optimization was about 1400 hours. After the optimization, the optimum geometry is selected from Pareto-optimal front solutions of the last iteration with the smallest surge mass flow.

4.2. Results and Discussions. The overall performances of baseline impeller and optimal impeller are presented in Table 6. It shows an improvement of both total pressure ratio

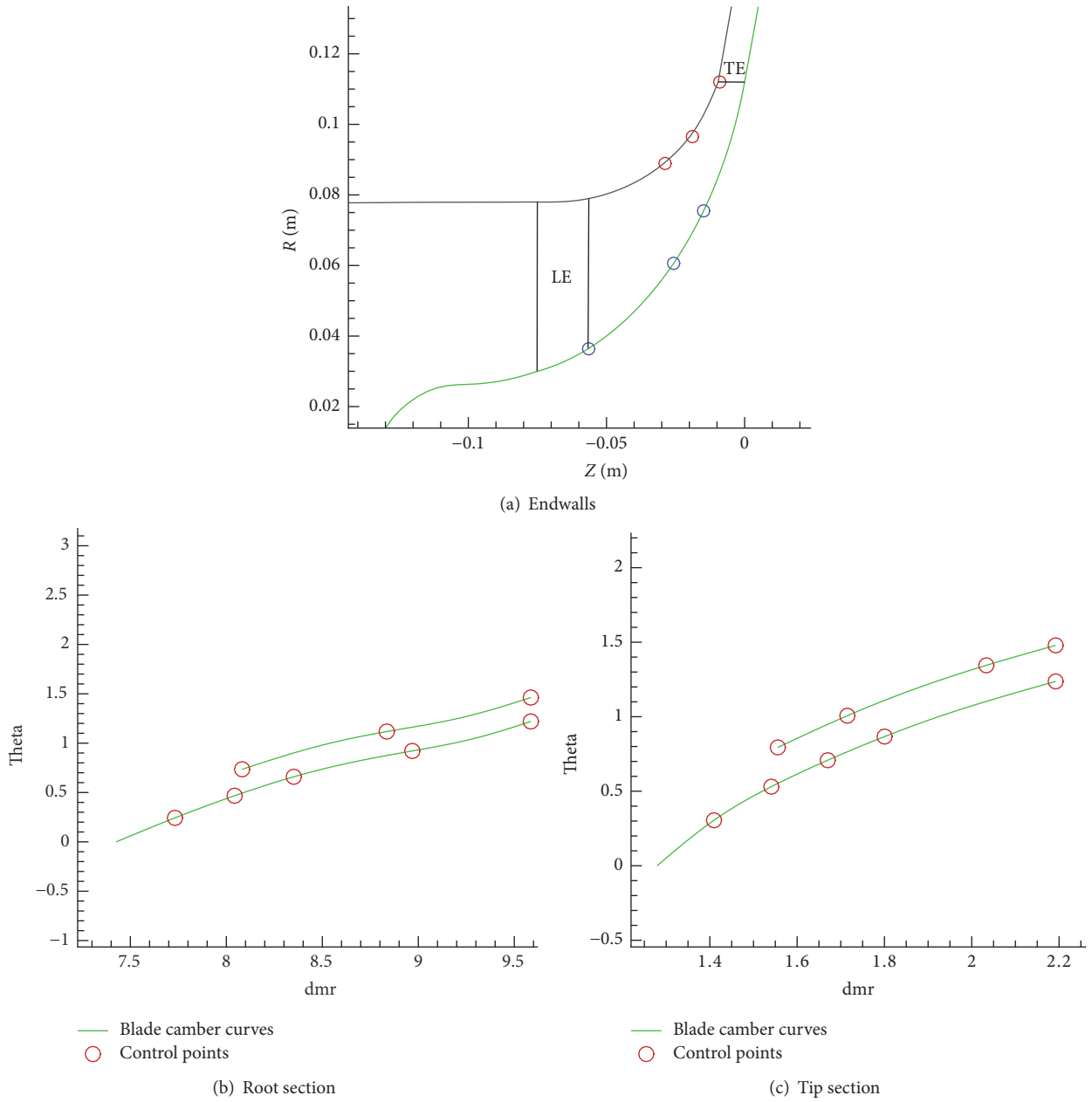


FIGURE 14: Active variables of endwalls and blade camber curves in final design space.

(by 5.3%) and isentropic efficiency (by 1.9%). Meanwhile, surge margin shows a considerable improvement by 6.8% while choke mass flow rises by 1.4% as well. The whole design speed line at 50000 rpm shows improvements for all the 4 objectives.

Figure 16 compares the performances of the optimal impeller with the baselines at three speeds of 50000 rpm, 40000 rpm, and 30000 rpm. At all speeds, compressor surge is improved. Combined with a higher choke flow at the highest speed, this makes the new design particularly suitable for turbocharger application where a wide flow range is required and choke flow at low pressure ratios is relatively

TABLE 6: The overall performances of baseline and optimal impellers at 50000 rpm.

Parameters	Baseline	Optimal	Improvement
$\epsilon_{tot,design}$	5.7	6.0	5.3%
$\eta_{is,design}$ (%)	80.0	81.5	1.9%
\dot{m}_{surge} (kg/s)	2.37	2.21	6.8%
\dot{m}_{choke} (kg/s)	2.87	2.91	1.4%

unimportant. Compressor peak efficiency and peak pressure ratio both increase at the off-design speeds.

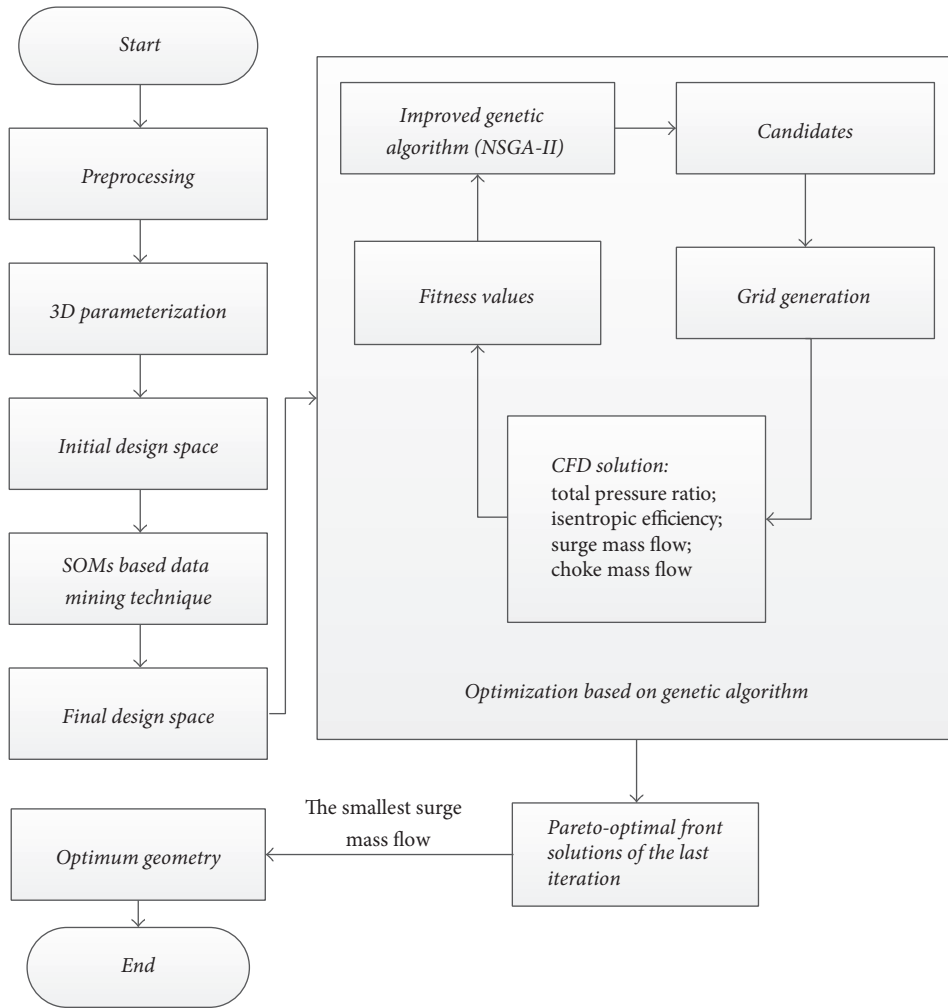


FIGURE 15: Flow chart of multipoint, multiobjective optimization method.

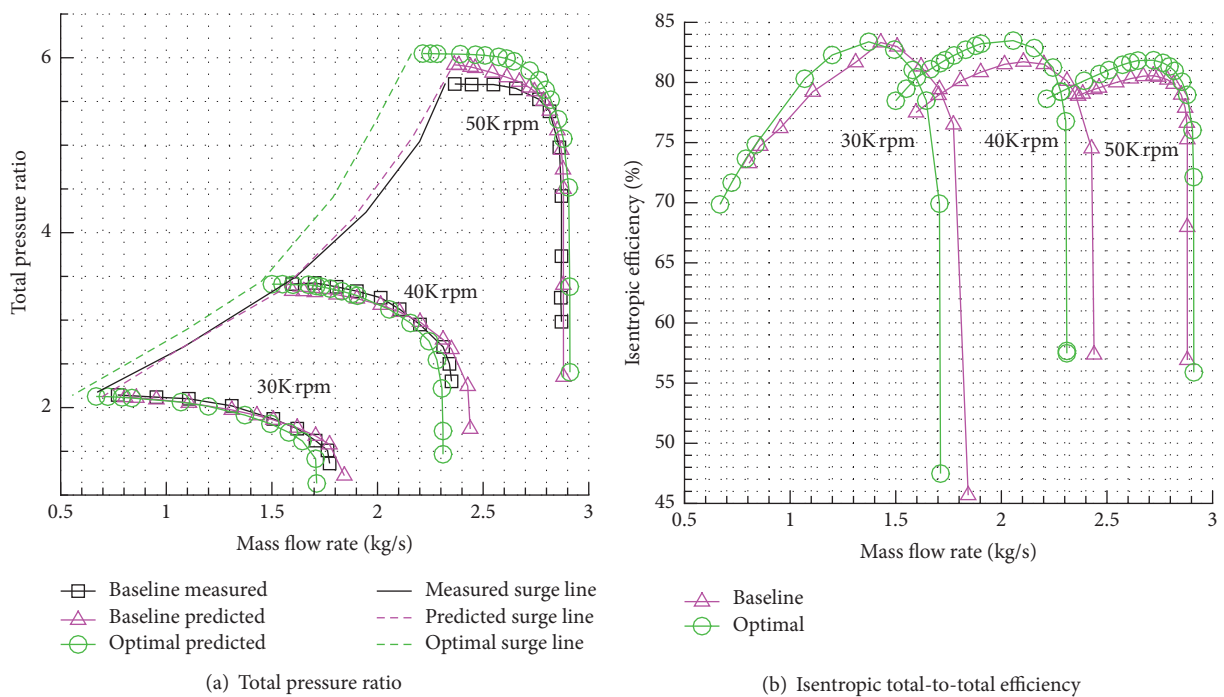


FIGURE 16: Comparison of off-design performance between baseline and optimal impellers.

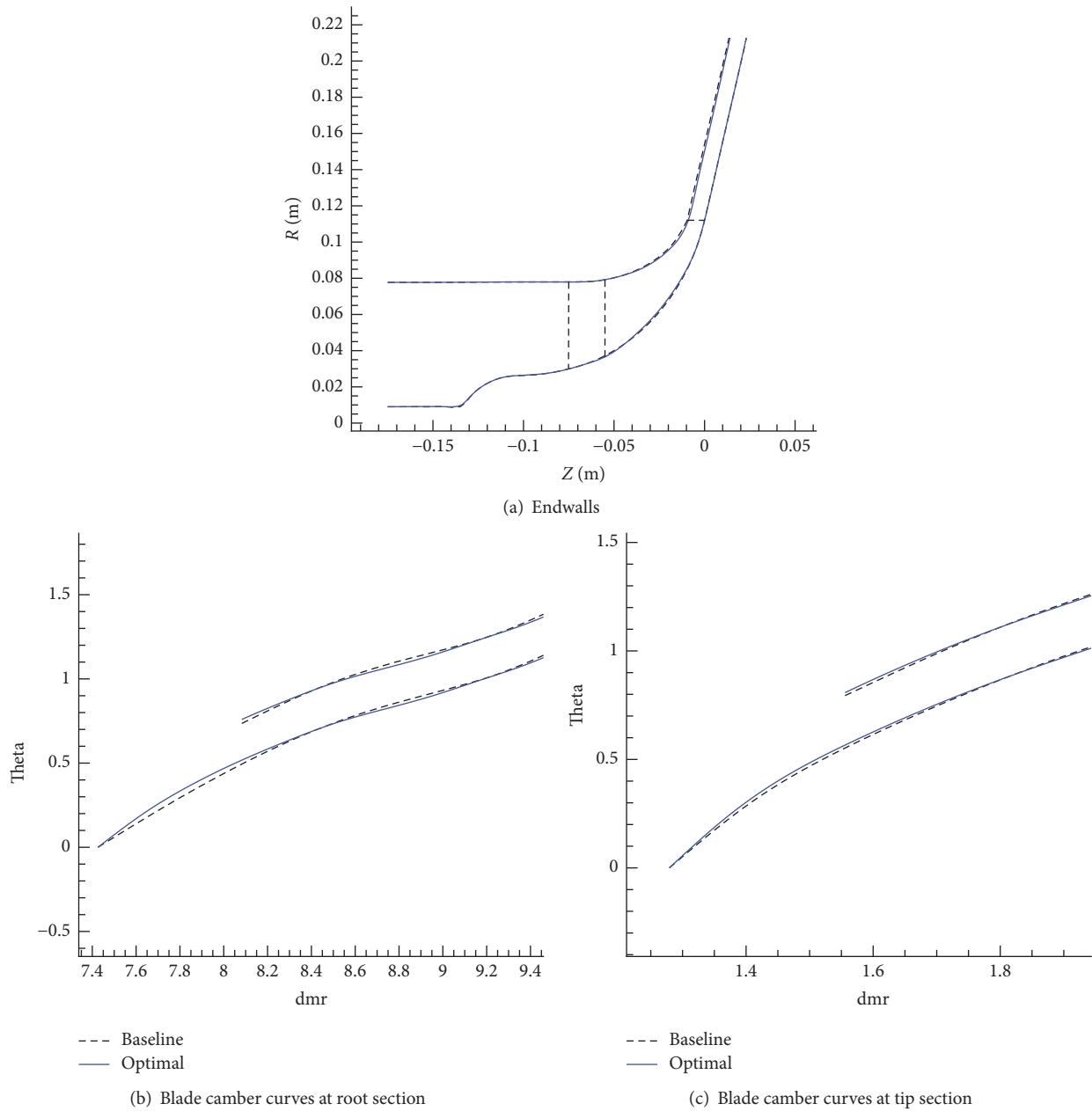


FIGURE 17: Comparison of geometry between baseline and optimal impeller.

These results demonstrate the power of this multipoint and multiobjective optimization method. A single-point optimization is less likely to get similar results. Note that this multipoint and multiobjective optimization is only conducted at design shaft speed (50000 rpm), and it could further improve off-design performance if the same technique is applied to both design and off-design speeds. This will significantly increase computational time and resources (about 3 times of this study). A trade-off is needed between the effort and the gains.

Figure 17 compares the geometry of the baseline and the optimal impeller. Figure 17(a) shows that the meridional

passage (variable 22) is reduced after the inducer throat in the optimal impeller. This explains why the choke flow of the impeller is reduced at the two lower speeds but not at the highest speed. At the low pressure ratios, exducer passage area also plays a rule in impeller choking while inducer throat alone dictates the impeller choke flow at high speeds. Figures 17(b) and 17(c) show the profile or camber changes of the full and splitter blades at root and tip sections. At the leading edge of the full blade (variables 44 and 52), both sections display a larger blade angle and higher blade turning, contributing to a higher efficiency and a smaller inducer area that is unfavourable for surge. The reduction of full blade throat is

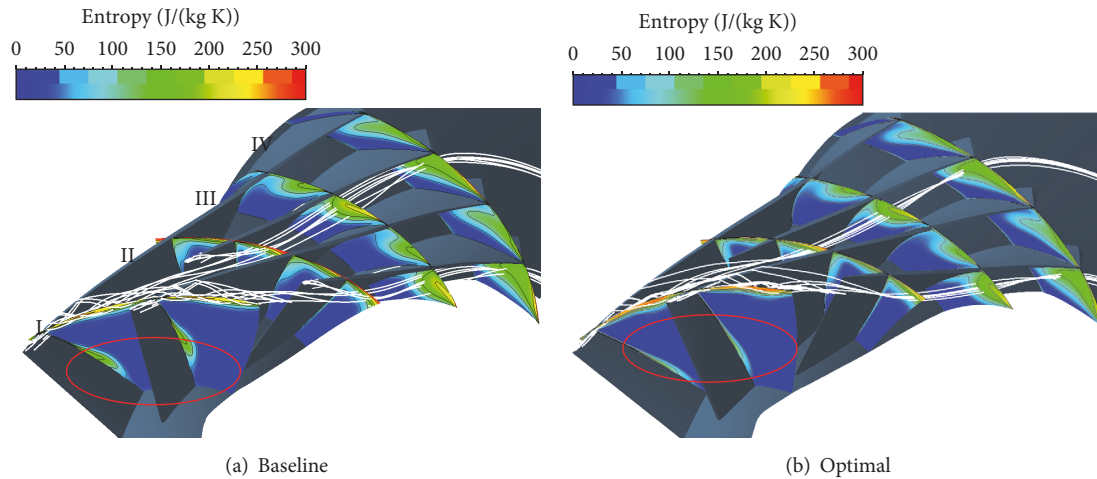


FIGURE 18: Entropy distributions at streamwise sections and streamlines.

compensated by a more open splitter (variables 59 and 64). The compressor stability is improved by the reduced impeller tip width (variable 33) and a smaller diffuser gap.

The backsweep angles (variables 50 and 63) are slightly reduced in the optimal impeller at its hub for both full blade and splitter blade, and this increases impeller work and pressure ratios. Because the same angle is not reduced at the shroud, the reduction at the hub decreases the diffusion imbalance between the shroud and the hub, resulting in more uniform impeller outflow. This compensates the higher diffuser inlet velocity caused by the reduced hub backsweep angle.

It is concluded that the design variables' optimization for a better performance corresponds to the analysis in SOM. It proves that SOM analysis is effective in extracting the key design variables and their effects, and the proposed optimization method was able to find a proper trade-off between all the objectives.

The flow field at design operating condition is analyzed. Figure 18 presents the comparison of entropy distributions at different streamwise sections and streamlines of tip leakage between the baseline and optimal impeller. In section I, a large high entropy region is found at midspan near suction side (circled in red) of the baseline impeller, and the corresponding area in the optimal impeller is considerably smaller. This is due to the weaker and detached LE shockwave moving back toward LE; see Figure 19. While the higher blade turning of the new impeller at LE area strengthens the tip leakage flow and thus higher loss is found in the tip region at Section I, the loss stops at Section III.

From Figure 19 it can be seen that impeller exit flow is now more uniform circumferentially between the two flow channels.

Figure 20 presents the spanwise performance of the impeller 10 mm downstream from the impeller exit. It shows that both the total pressure ratio and the isentropic efficiency have increased in the regions ranging from the hub to 80% span but reduced near the shroud.

5. Conclusions and Remarks

A multipoint and multiobjective design optimization strategy of centrifugal impeller is proposed by integrating a genetic algorithm, 3D geometry parameterization, CFD tools, time series based surge detection method, and SOMs based data mining technique. This approach was successfully applied to high pressure ratio centrifugal impeller SRV2AB for higher total pressure ratio and better efficiency at design operating condition and smaller surge mass flow and larger choke mass flow at design speed. The main conclusions are drawn as follows:

(1) A time series based surge detection method was introduced. It uses autoregression to detect compressor instability and is independent of the impeller geometry, shaft speed, and boundary condition. This method was successfully applied to SRV2AB impeller surge prediction.

(2) By SOM-based data mining on initial design space, trade-off relations between objective functions and correlations among design variables and objective functions were visualized and analyzed. The key design variables were then identified and kept in the final design space.

(3) The optimization improves the overall performance of the impeller at whole design speed line and widens the compressor flow range. At off-design speeds and compressor efficiency, surge margin is also enhanced. The mechanism behind the performance improvement is further explained by combining geometry changes with detailed flow analysis.

The surge detection method still needs to be checked by experiment and by more applications. It is currently computational intensive. It essentially detects surge by the macroscopic time based signal instead of local flow features such as the development of stall cells, which may be more efficient. The method needs further refinement.

Another future work concerns with the method of selecting the data for data mining. Results of data mining techniques may depend on the used data. For the consistency of information obtained from data mining, a robust data selection method is necessary.

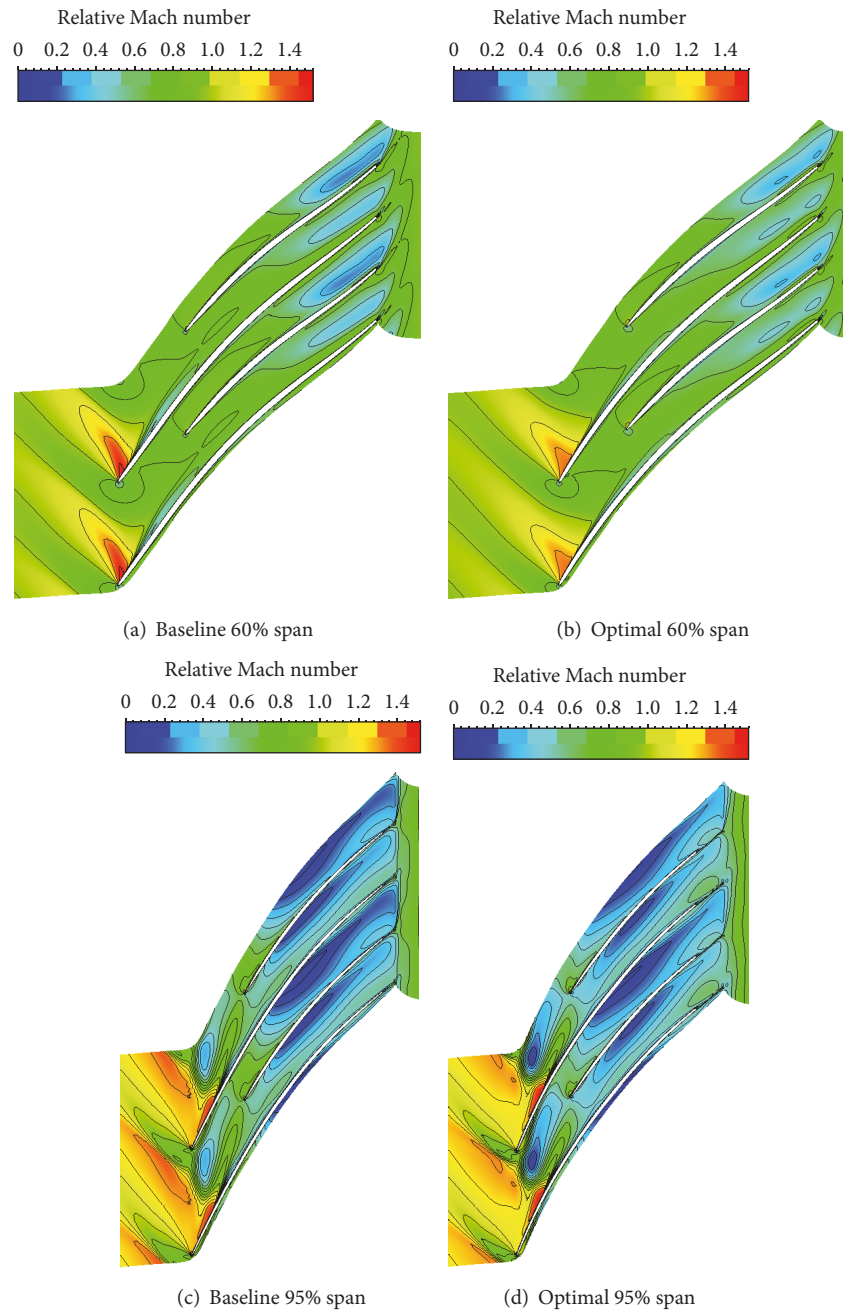


FIGURE 19: Relative Mach number contour at 60% and 95% spans.

Nomenclature

AR: Autoregressive processes
 ARMA: Autoregressive moving average processes
 a : Amplitude of time based signal
 a_t : White noise series
 deg: Degree
 GA: Genetic algorithm
 LE: Leading edge
 MA: Moving average processes
 \dot{m} : Mass flow rate

\dot{m}_{choke} : Choke mass flow
 \mathbf{m}_i : Weight vector
 \dot{m}_{surge} : Surge mass flow (last stable mass flow near surge condition)
 NID: Normally and independently distributed
 n : Shaft speed (rpm)
 P : Probability
 P_{c1} : Upper border of crossover probability
 P_{c2} : Lower border of crossover probability
 P_{m1} : Upper border of mutation probability
 P_{m2} : Lower border of mutation probability
 p : Pressure

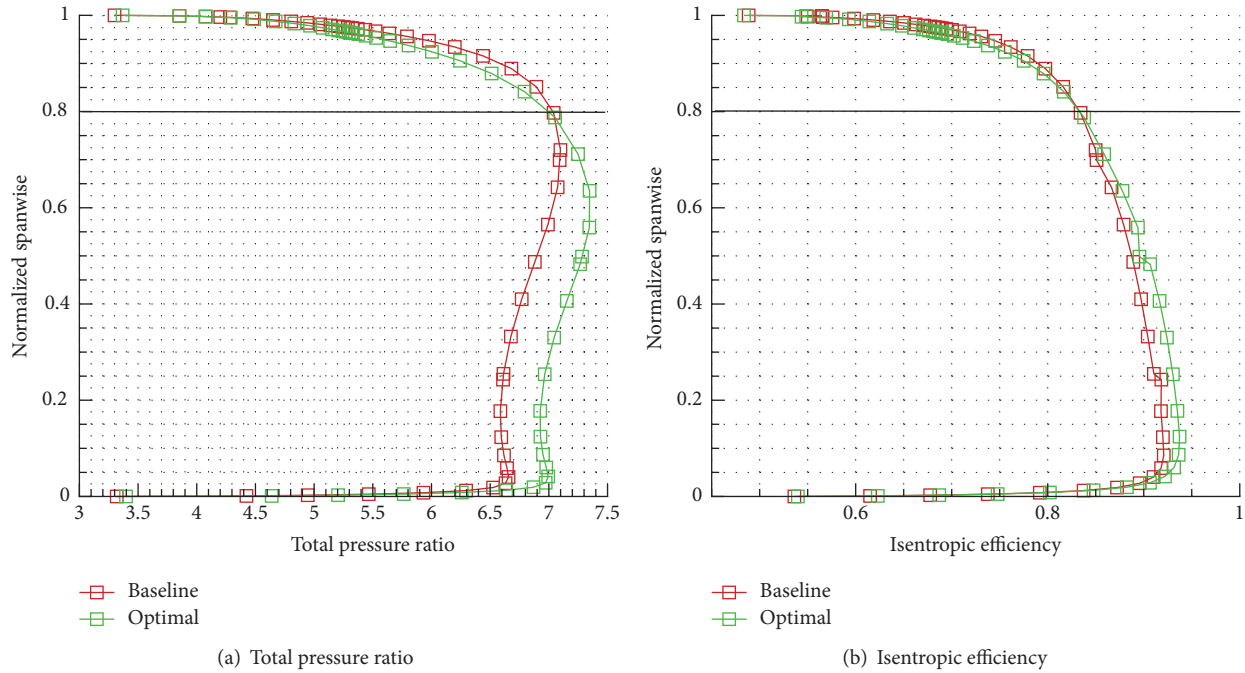


FIGURE 20: Spanwise performance 10 mm downstream of impeller.

- q : Order of AR model
- R : Radial coordination (mm)
- R_k : Autocovariance function
- SOM: Self-organization map
- TE: Trailing edge
- x_t : Original time series signal
- y_t : Zero-mean time series
- Z : Axial coordination (mm).

Greek Symbols

- δ : Upper border of variance in AR model
- ε : Total pressure ratio
- η : Isentropic efficiency
- θ : Azimuthal angle (rad)
- μ_x : Mean value
- ρ_k : Autocorrelation function
- σ^2 : Variance
- ϕ_i : Coefficients of AR model
- φ_{kk} : Partial autocovariance function.

Subscripts

- c : Crossover
- choke: Choke condition
- design: Design condition
- full: Full blade
- is: Isentropic
- m : Mutation
- root: Root section
- splitter: Splitter blade
- surge: Surge condition

- tot: Total conditions
- tip: Tip section.

Conflicts of Interest

The authors declare that there are no conflicts of interest regarding the publication of this paper.

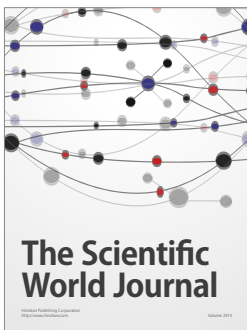
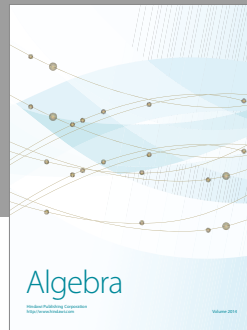
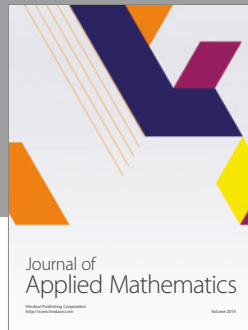
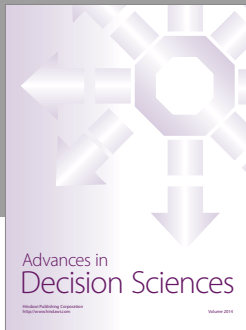
Acknowledgments

This research work is supported by National Natural Science Foundation of China (Grant no. 11672206) and State Key Laboratory of Internal Combustion Engine Burning (Grant no. K201607).

References

- [1] P. G. Tucker, "Computation of unsteady turbomachinery flows: part 1—progress and challenges," *Progress in Aerospace Sciences*, vol. 47, no. 7, pp. 522–545, 2011.
- [2] L. He and J. Yi, "Two-scale methodology for URANS/large eddy simulation solutions of unsteady turbomachinery flows," *Journal of Turbomachinery*, vol. 139, no. 10, p. 101012, 2017.
- [3] D. Pasquale, G. Persico, and S. Rebay, "Optimization of turbomachinery flow surfaces applying a CFD-based throughflow method," *Journal of Turbomachinery*, vol. 136, no. 3, p. 031013, 2014.
- [4] R. Hunziker, H. Dickmann, and R. Emmrich, "Numerical and experimental investigation of a centrifugal compressor with an inducer casing bleed system," *Journal of Power and Energy*, vol. 215, no. 6, pp. 783–791, 2005.
- [5] H. Krain, "Review of centrifugal compressor's application and development," *Journal of Turbomachinery*, vol. 127, no. 1, pp. 25–34, 2005.

- [6] Z. Guo, Z. Zhou, L. Song, J. Li, and Z. Feng, "Aerodynamic Analysis and Multi-Objective Optimization Design of a High Pressure Ratio Centrifugal Impeller," in *Proceedings of the ASME Turbo Expo 2014: Turbine Technical Conference and Exposition*, p. V02DT42A013, Düsseldorf, Germany, 2014.
- [7] T. Verstraete, Z. Alsalihi, and R. A. Van den Braembussche, "Multidisciplinary optimization of a radial compressor for microgas turbine applications," *Journal of Turbomachinery*, vol. 132, no. 3, pp. 1291–1299, 2007.
- [8] K. Hyun-Su, S. Yoo-June, and K. Youn-Jea, "Optimal design of impeller for centrifugal compressor under the influence of fluid-structure interaction, ASME/JSME/KSME joint fluids engineering conference," in *Proceedings of the Optimal Design of Impeller for Centrifugal Compressor Under the Influence of Fluid-Structure Interaction, ASME/JSME/KSME Joint Fluids Engineering Conference*, p. 02248, 2015.
- [9] A. Demeulenaere, J. Bonaccorsi, D. Gutzwiller, L. Hu, and H. Sun, "Multi-disciplinary multi-point optimization of a turbocharger compressor wheel," in *Proceedings of the ASME Turbo Expo 2015: Turbine Technical Conference and Exposition*, p. V02CT45A020, Montreal, Quebec, Canada, 2015.
- [10] M. Pini, G. Persico, and V. Dossena, "Robust adjoint-based shape optimization of supersonic turbomachinery cascades," in *Proceedings of the ASME Turbo Expo 2014: Turbine Technical Conference and Exposition*, p. V02BT39A043, Düsseldorf, Germany, 2014.
- [11] Z. Guo, L. Song, J. Li, G. Li, and Z. Feng, "Research on meta-model based global design optimization and data mining methods," in *Proceedings of the ASME Turbo Expo 2015: Turbine Technical Conference and Exposition*, p. V02CT45A007, Montreal, Quebec, Canada, 2015.
- [12] S. Jeong, K. Chiba, and S. Obayashi, "Data mining for aerodynamic design space," *Journal of Aerospace Computing Information & Communication*, vol. 2, no. 11, pp. 452–469, 2005.
- [13] N. González Díez, J. P. Smeulers, L. Tapinassi, A. S. Del Greco, and L. Toni, "Predictability of rotating stall and surge in a centrifugal compressor stage with dynamic simulations," in *Proceedings of the ASME Turbo Expo 2014: Turbine Technical Conference and Exposition*, p. V02DT44A032, Düsseldorf, Germany, 2014.
- [14] J. Galindo, J. Serrano R, C. Guardiola, and C. Cervelló, "Surge limit definition in a specific test bench for the characterization of automotive turbochargers," *Experimental Thermal & Fluid Science*, vol. 30, no. 5, pp. 449–462, 2006.
- [15] S. Marelli, C. Carraro, G. Marmorato, G. Zamboni, and M. Capobianco, "Experimental analysis on the performance of a turbocharger compressor in the unstable operating region and close to the surge limit," *Experimental Thermal & Fluid Science*, vol. 53, no. 2, pp. 154–160, 2014.
- [16] R. Yao and N. Pakzad S, "Autoregressive statistical pattern recognition algorithms for damage detection in civil structures," *Mechanical Systems & Signal Processing*, vol. 31, no. 8, pp. 355–368, 2012.
- [17] L. Fanyu, L. Jun, D. Xu, S. Dakun, and S. Xiaofeng, "Stall warning approach with application to stall precursor-suppressed casing treatment," in *Proceedings of the ASME Turbo Expo 2016: Turbomachinery Technical Conference and Exposition*, p. V02DT44A038, Seoul, South Korea, 2016.
- [18] C. Hah, D. C. Rabe, and A. R. Wadia, "Role of tip-leakage vortices and passage shock in stall inception in a swept transonic compressor rotor," in *Proceedings of the ASME Turbo Expo 2004: Power for Land, Sea, and Air*, pp. 545–555, Vienna, Austria, 2004.
- [19] C. Hah, J. Bergner, and H. Schiffer, "Short length-scale rotating stall inception in a transonic axial compressor: criteria and mechanisms," in *Proceedings of the ASME Turbo Expo 2006: Power for Land, Sea, and Air*, pp. 61–70, Barcelona, Spain, 2006.
- [20] X. Zheng, Z. Sun, T. Kawakubo, and H. Tamaki, "Experimental investigation of surge and stall in a turbocharger centrifugal compressor with a vaned diffuser," *Experimental Thermal and Fluid Science*, vol. 82, pp. 493–506, 2017.
- [21] G. Eisenlohr, H. Krain, F. Richter, and V. Tiede, "Investigations of the flow through a high pressure ratio centrifugal impeller," in *Proceedings of the ASME Turbo Expo 2002: Power for Land, Sea, and Air*, pp. 649–657, Amsterdam, The Netherlands, 2002.
- [22] M. Zangeneh, N. Amarel, K. Daneshkhhah, and H. Krain, "Optimization of 6.2:1 pressure ratio centrifugal compressor impeller by 3D inverse design," in *Proceedings of the ASME 2011 Turbo Expo: Turbine Technical Conference and Exposition*, pp. 2167–2177, Vancouver, British Columbia, Canada, 2011.
- [23] F. Ning and L. Xu, "Numerical investigation of transonic compressor rotor flow using an implicit 3d flow solver with one-equation spalart-allmaras turbulence model," in *Proceedings of the ASME Turbo Expo 2001: Power for Land, Sea, and Air*, p. V001T03A054, New Orleans, LA, USA, 2001.
- [24] D. X. Wang and X. Huang, "Solution stabilization and convergence acceleration for the harmonic balance equation system," *Journal of Engineering for Gas Turbines & Power*, 2017.
- [25] Ansys Fluent 16.0 User's Guide, "Ansys Inc," 2015.
- [26] X. Li, Y. Zhao, Z. Liu, and H. Chen, "The optimization of a centrifugal impeller based on a new multi-objective evolutionary strategy," in *Proceedings of the ASME Turbo Expo 2016: Turbomachinery Technical Conference and Exposition*, p. V02CT39A022, Seoul, South Korea, 2016.
- [27] K. J. Cios, W. Pedrycz, and R. W. Swiniarski, *Data Mining Methods for Knowledge Discovery*, Kluwer Academic Publisher, 1998.



Hindawi

Submit your manuscripts at
<https://www.hindawi.com>

